Soft Matter

Cite this: *Soft Matter*, 2011, **7**, 10135

www.rsc.org/softmatter

PAPER

Interaction of bi-dispersed particles with contact line in an evaporating colloidal drop

Viral H. Chhasatia and Ying Sun*

Received 21st July 2011, Accepted 23rd August 2011
DOI: 10.1039/c1sm06393f

The deposition behavior of an inkjet-printed aqueous colloidal mixture of micro- and nanoparticles onto a glass substrate with systematically varied wettability has been investigated using fluorescence microscopy. Real-time bottom-view images show that particles inside an evaporating drop rearrange themselves near the drop contact line according to their sizes, where smaller particles tend to deposit closer to the contact line compared to the larger ones. By increasing substrate wettability, particles in the bi-dispersed mixture can be further separated compared to those on substrates of poor wettability. This is primarily because, during different stages of evaporation, the interplay of surface tension, drag due to evaporative flow, and particle–substrate interactions rearrange particles inside a colloidal drop near the contact line region. Forces acting on particles determine the extent to which particles enhance contact line pinning, which ultimately determines the final deposition morphology of particles from a bi-dispersed colloidal mixture.

1. Introduction

Evaporation of a sessile drop containing pure liquid usually occurs in three distinct stages,[1] first the constant contact area mode where the contact line (CL) is pinned, followed by the constant contact angle stage where the drop contact angle reaches below the static receding contact angle and the CL depins, and finally the mixed mode where both the contact area and contact angle decrease. The addition of particles in a colloidal drop extends the lifespan of the constant contact area stage. This is due to the fact that accumulation of particles along the drop edge driven by evaporation enhances CL pinning. The decrease in the contact angle due to evaporation is offset by the increase in the contact angle caused by new protruding particles to the CL.[2] This delay of the second and third stages of evaporation in the presence of particles causes the well-known coffee-ring effect. Previous studies within our group,[3] as well as others,[4] have demonstrated that the particle size and contact angle between the carrier liquid and substrate determine the distance away from the CL a particle gets deposited. Smaller particles move closer to the pinned CL compared to larger particles due to the liquid meniscus physically restricting the movement of larger particles.

The co-existence of micro- and nanoparticles further complicates the interactions between particles and the CL. Increasing interest in using a receding liquid–vapor interface to guide size-dictated particle separation in evaporating drops has been developed in recent years.[2,5–12] For example, effective isolation of virus, bacteria, and biological cells from body fluids is important in improving the sensitivity and accuracy of disease detection.[6] In the meantime, this size-induced particle separation presents a new challenge to the uniform deposition of inkjet-printed functional materials because particles of different sizes can aggregate at different locations in the final deposition. Weon and Je[11] studied the deposition of a colloidal drop containing bi-dispersed particles and showed that the liquid–air interface forms a wedge in the CL region and separates particles according to their sizes in an evaporating drop. The particle separation distance, x, between the outermost large and small particles is given by $x = r/\tan(\theta/2)$, where r is the radius of the particle and θ is the angle of the CL wedge. Evolution of the contact angle with time can be described by the following empirical power-law dependence:[13]

$$\theta(t) = \theta_0(t_0 - t)^{\beta} \quad (1)$$

where t_0 is the total time for evaporation, θ_0 and β are fitting parameters. Birdi *et al.*[14] explained that, for a drop with a pinned CL, the height of the drop decreases linearly with time for a drop of a low contact angle ($\sim$<30°). The increase in the separation distance with time can thus be simplified as:[11]

$$x(t) = \left(\frac{2r}{\theta_0}\right)(t_0 - t)^{-\beta} \quad (2)$$

It has been observed[6,9,11] that, for a colloidal drop containing micro- and nanoparticles, the micron-sized particles move radially inward during the final stage of evaporation whereas the nano-sized particles remain at the drop CL. Wong *et al.*[9] explained that, for a pinned CL, particles can either remain at the

Department of Mechanical Engineering and Mechanics, Drexel University, Philadelphia, PA, 19104, USA. E-mail: ysun@coe.drexel.edu; Fax: +1 (215)895-1478; Tel: +1(215)895-1373

CL or move radially inward during drop evaporation, depending upon the balance between the attraction forces among the particles and the surface tension force acting on particles. For a large number of particles forming a monolayer along the CL, the attraction forces between particles can be stronger than the surface tension force and the particles remain pinned at the CL.

Previous studies on the deposition of bi-dispersed particles from evaporating colloidal drops[5–12] suggest that the liquid–vapor interface forms a wedge at the drop CL and this CL wedge prevents particles from protruding through the liquid–vapor interface. Except for Wong *et al.*,[9] the research focus so far has been on particle separation on hydrophilic substrates with a pinned CL inside a micron-sized sessile drop. In this paper, we present experimental results for inkjet-printed, evaporating aqueous colloidal drops containing 100 nm and 1.1 μm particles deposited on glass substrates of varying wettabilities. Picolitre colloidal drops produced by an inkjet printer represent a common drop size widely used for high-resolution materials printing applications. In such length scales, capillary and evaporation are the dominating mechanisms, whereas gravitational and inertia effects are negligible. The forces acting on the micro- and nanoparticles, particle separation distance, drop evaporation and particle dynamics, as well as pinning and depinning of the CL have been investigated on systematically varied substrates with a static contact angle ranging from 5° to 95° (measured using a pure water drop to eliminate the effect of particles). We also report the possibility of micron-sized particles protruding through the liquid–vapor interface for the case of a hydrophilic substrate, where the actual distance between the outermost micro- and nanoparticles is less than the value suggested by the CL wedge assumption.

2. Experimental details

To obtain substrates with varying degrees of wettability, glass microscope cover slips (Bellco, ~150 μm thick) underwent a sequence of cleaning, silanization, and plasma treatment. First, substrates were cleaned by sonicating in Sparkleen-DI water solution, ethanol and acetone for fifteen minutes each, immediately dried in a stream of compressed air and treated with Argon gas plasma (2 minutes each side at 18 W and 250 mtorr, Harrick Plasma PDC-32G). Silanization consisted of soaking the substrates for one hour in a 5 mM solution of octadecyltrichlorosilane (OTS) in hexane (both from Sigma Aldrich and used as received). This silanization was carried out inside a dry glove box with a controlled N_2 atmosphere to minimize excessive polymerization of the water-sensitive OTS molecules. Varying degrees of wettability (different receding contact angles θ_{RCA}) were obtained on the substrates by subjecting the already silanized surfaces to time-varying treatments of Ar plasma. In the current study, the time of treatment from 2 to 60 seconds at a power level of 6 W and 250 mtorr Argon pressure was used to produce systematically varied wettability of glass surfaces with no measurable change in surface roughness. Static advancing (θ_{ACA}) and static receding (θ_{RCA}) contact angles of the substrates were measured by using a goniometer setup using a micro-pipetted droplet containing DI-water to minimize the effects of evaporation and the presence of particles.

A colloidal mixture of carboxylate-modified polystyrene fluorescent beads of 100 nm and 1.1 μm diameter in DI-water, each 0.5% by volume, was used in our inkjet printing experiments. Picolitre drops were generated using a piezoelectric-driven inkjetting nozzle (MicroFab MJ-AL01). A high resolution (0.5 μm per pixel) image acquisition system, consisting of a SensiCam QE CCD camera (Romulus, Michigan) and a Navitar 12× Zoom lens (Rochester, New York), was synchronized by using a delay generator (SRS DG645, Sunnyvale, California) with a halogen strobe light and the drop ejection to form a drop side-view observation system. Particle motion and deposition inside the colloidal drop were observed using a Zeiss inverted fluorescence microscope (Thornwood, New York) with a 40× objective and bottom-view images were captured by a Sony XCL-5005CR CCD camera (Park Ridge, New Jersey) at 10 frames per second. The ambient temperature and humidity were kept at 22 °C and 20% relative humidity for all experiments. Details of the experimental setup are described elsewhere.[15] Contact angle measurements based on side-view images were carried out using IMAGEJ (http://rsbweb.nih.gov/ij/) assuming that the drop interface remains a spherical cap at all times. Neglecting gravitational distortion of the drop shape is well justified because the Bond number in our printed drops is less than 0.005.

3. Forces acting on particles near a CL

As shown in Fig. 1a, colloidal particles in an evaporating drop experience van der Waals and electrostatic interactions with other particles, as well as with the substrate near a CL. Here, we focus on the regime of large Peclet numbers (the ratio of shear-driven to Brownian motion at the particle scale) and neglect the random force causing Brownian motion and the non-DLVO forces acting on the particles.

A. van der Waals interaction

The particle–substrate van der Waals force, F_{wps}, between particles and the substrate in a fluid medium is given by:[16]

$$F_{wps} = \frac{2nA_{123}r^3}{3z^2(z+2r)^2} \quad (3)$$

where n is the number of particles, A_{123} is the Hamaker constant where the subscript 1 denotes the particle, 2 is the substrate, 3 denotes the fluid medium, and z is the particle–substrate separation distance. This particle–substrate adhesive force attempts to keep the particles near the substrate. Also, the van der Waals force acting among particles in a fluid medium, F_{wpp}, can be calculated by:[16]

$$F_{wpp} = \frac{nA_{131}r}{12z^2} \quad (4)$$

where A_{131} is the Hamaker constant between particles in a fluid.

B. Electrostatic interaction

The electrostatic force acting between particles and the substrate in a fluid medium, F_{eps}, is given by:[9]

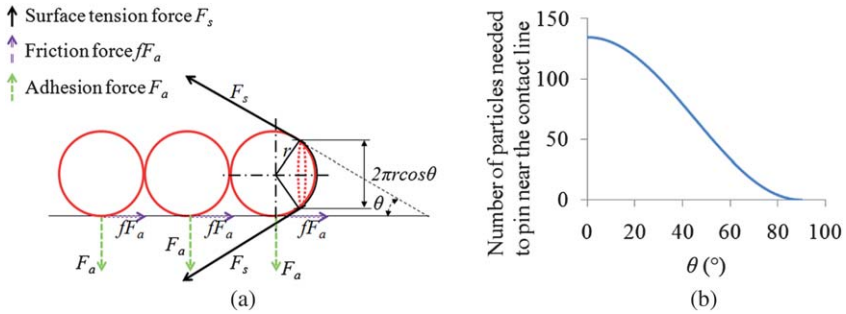

Fig. 1 Forces acting on particles near a CL. (a) Schematic of surface tension, adhesion, and friction forces acting on particles near a CL and (b) the number of particles required to pin themselves near the contact line as a function of the contact angle.

$$F_{eps} = -2n\pi r\varepsilon\kappa \frac{\left[\phi_1^2 + \phi_2^2 - 2\phi_1\phi_2 \exp(\kappa z)\right]}{\left[\exp(2\kappa z) - 1\right]} \quad (5)$$

where ε is the fluid permittivity, κ is the reciprocal of Debye length, ϕ_1 is the surface potential for particles, and ϕ_2 is the surface potential for the substrate. The electrostatic force acting among particles in a fluid medium, F_{epp}, is given by:[17]

$$F_{epp} = -\frac{\varepsilon r\phi_1^2}{4} \frac{2\kappa \exp(\kappa z)}{\exp(2\kappa z) + 1} \quad (6)$$

Note that both particle–substrate and particle–particle electrostatic forces are repulsive.

C. Forces acting on particles parallel to substrate

The particle motion near a CL is a result of the interplay between various interaction forces as depicted in Fig. 1a. For example, the surface tension force acting on the particles near the CL tends to move them away from the CL, whereas the static friction force, to a certain extent, keeps particles stationary. The total attractive force, F_a, acting between particles and the substrate can be calculated by summing up the van der Waals, electrostatic, and net gravitational forces:[7]

$$F_a = F_{wps} + F_{eps} + F_g \quad (7)$$

For neutrally buoyant particles, the net gravitational force, F_g, can be neglected. The total attractive force, F_a, induces a static friction force that prevents particles from moving parallel to the substrate away from the CL. The static friction force, fF_a, can be calculated by estimating the friction coefficient, f, based on the ratio of the drag force, F_d, to the attractive force, where the drag force acting on the particles is given by:[7]

$$F_d = 6\pi r\eta v \quad (8)$$

Here η is the dynamic viscosity of the fluid and v is the velocity of the evaporative flow. In addition, particles near the liquid–vapor interface experience a surface tension force, F_s, given by:[7]

$$F_s = 2\pi r\sigma\cos\theta \quad (9)$$

where σ is the surface tension of the liquid–vapor interface.

D. Estimation of forces acting on polystyrene particles in an aqueous colloidal drop on glass

Now, we estimate the van der Waals, electrostatic, surface tension, and drag forces acting on polystyrene particles in an aqueous evaporating colloidal drop on a glass substrate. Values of all constants used in the force calculations are listed in Table 1 and the resulting forces are listed in Table 2. For a substrate with a contact angle of 30°, our estimation suggests that it requires about 101 particles to pin themselves near the CL regardless of the particle radius. Note that, the forces acting among particles are in different directions and much weaker compared to particle–substrate interactions, and are therefore neglected in our estimation. Fig. 1b shows the number of particles required to pin themselves as a function of the contact angle. As the horizontal component of surface tension force, $F_s\cos\theta$, decreases with the increase in the contact angle, less particles are required to overcome the surface tension force and pin themselves near the CL. In addition, both friction and surface tension forces depend upon the radius of the particle, and hence their ratio remains roughly the same regardless of the particle radius. However, for micro- and nanoparticles of the same volume fraction, because the total number of nanoparticles is much larger than that of microparticles, nanoparticles can get closer to the CL and facilitate CL pinning much easier than their microparticle counterparts.

4. Results and discussion

Particle deposition morphology of colloidal drops depends strongly upon substrate wettability,[19] which changes the duration of the three evaporation modes and the interplay between surface tension, drag, electrostatic, and van der Waals forces acting on both the micro- and nanoparticles in an evaporating colloidal drop. Fig. 2 shows the particle separation distance between the outermost micro- and nanoparticles for four different substrates with the static receding contact angle, θ_{RCA}, ranging from 0 to 85°. It is shown that the particle separation increases significantly as the contact angle decreases due to changes in drop evaporation modes and interaction forces acting on the particles. The contact line radii *versus* time for an evaporating drop on substrates of θ_{RCA} = 80°, 55°, 30°, 10°, and 0° are shown in Fig. 3. With the increase in substrate wettability, the drop evaporation time decreases and the constant contact area stage becomes increasingly dominant. For the cases of $\theta_{RCA} = 0°$ and 10°, the drops remain pinned during the entire evaporation process. A distinct three-mode evaporation process, including the constant contact area, constant contact angle, and mixed modes, is observed for $\theta_{RCA} = 30°$. For the cases of $\theta_{RCA} = 55°$ and 80°, the constant contact angle mode dominates evaporation. Different microflow patterns inside the drop for each of the

Table 1 Parameters used in force calculations of aqueous polystyrene suspensions depositing on glass

Symbol	Physical parameter	Value	Unit
A_{123}	Hamaker constant between the polystyrene particle and glass in water	3×10^{-20} (ref. 9)	J
A_{131}	Hamaker constant between polystyrene particles in water	1×10^{-20} (ref. 18)	J
σ	Surface tension of water	0.072	N m^{-1}
z	Minimum separation distance	0.4×10^{-9} (ref. 9)	m
ε	Permittivity of water	7×10^{-10}	F m^{-1}
ϕ_1	Surface potential of polystyrene	15 (ref. 9)	mV
ϕ_2	Surface potential of glass	−40 (ref. 9)	mV
η	Dynamic viscosity of water	0.9	cP
v	Velocity of water in evaporating drop	0.2	m s^{-1}
κ	Reciprocal of the Debye length	$(430 \times 10^{-9})^{-1}$ (ref. 9)	m^{-1}

Table 2 Interaction forces acting on particles in an aqueous colloidal drop containing polystyrene particles on glass

Name	For $r =$ 550×10^{-9} m	For $r =$ 50×10^{-9} m
F_{wps}	1.72×10^{-8} N	1.55×10^{-9} N
F_{wpp}	2.87×10^{-9} N	2.6×10^{-10} N
F_{eps}	-6.4×10^{-9} N	-5.81×10^{-10} N
F_{epp}	-5.04×10^{-14} N	-4.58×10^{-15} N
F_a	1.08×10^{-8} N	9.7×10^{-10} N
F_d	1.85×10^{-9} N	1.68×10^{-10} N
Friction coefficient, $f = F_d/F_a$	0.17	0.17
Friction force, fF_a	1.85×10^{-9} N	1.68×10^{-10} N
F_s ($\theta = 30°$)	2.15×10^{-7} N	1.96×10^{-8} N
Number of particles required to pin, $n = F_s\cos\theta/fF_a$	101	101

three evaporation modes significantly influence the deposition morphology of bi-dispersed particles on substrates of varying wettabilities.

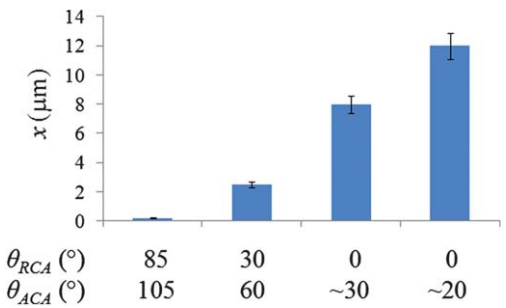

Fig. 2 Final separation distance between outermost micro- and nanoparticles (x) as a function of substrate wettability indicated by static advancing (θ_{ACA}) and static receding (θ_{RCA}) contact angles. In columns three and four, θ_{ACA} decreases while θ_{RCA} remains 0°.

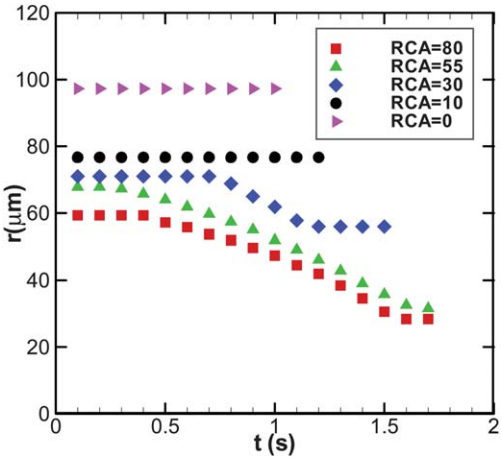

Fig. 3 Contact line radius *versus* time for evaporating drops on substrates of different wettabilities. Colloidal suspension was formed from 0.1 and 1.1 μm polystyrene beads with a particle volume fraction of 0.5% each in water and a drop diameter before impact on glass substrates was 80 μm.

The scaled radial positions of microparticles *versus* time in an evaporating drop on substrates of $\theta_{RCA} = 55°$ and 10° are shown in Fig. 4. Four representative microparticles initially located at 25%, 50%, 75%, and ~100% (outermost microparticle) of the initial drop CL radius r_{CL0} are selected. For the case of $\theta_{RCA} = 55°$ where the constant contact angle mode dominates the drop evaporation process, particles inside the drop move only slightly towards the CL until being collected as the CL recedes (Fig. 4a). Whereas, for the case of $\theta_{RCA} = 10°$, the CL remains pinned during the entire evaporation process. Microparticles inside the drop move towards the pinned CL due to evaporatively driven flow, whereas those microparticles very close to the drop edge move slightly inward under the surface tension of the water–air interface as nanoparticles pin the contact line.

In the following, we describe the separation mechanism of bi-dispersed particles in three distinct groups based on the receding contact angle of the substrate, from mixed, to partially separated, and finally to completely separated as θ_{RCA} decreases.

A. $\theta_{RCA} > 45°$ (mixed)

For substrates with a receding contact angle higher than 45°, the first two stages of evaporation are clearly observed, as shown in side-view snapshots in Fig. 5a and c for the cases of $\theta_{RCA} = 80°$ and $\theta_{RCA} = 55°$, respectively. In general, the higher the receding contact angle, the smaller footprint the particles deposit on the substrate. In the constant contact area stage of evaporation, colloidal particles are advected to the pinned CL due to the evaporatively driven flow. Once the contact angle, θ, reaches the static receding contact angle, θ_{RCA}, the CL starts receding. At the constant contact angle stage, evaporation occurs uniformly along the liquid–vapor interface and the contact area of the drop decreases linearly with time.[19] The lack of particle motion towards the CL at this stage prevents particles from accumulating near the CL to a level required for them to pin (shown in Fig. 1b). Micro- and nanoparticles accumulate near the receding liquid–vapor interface and remain mixed as shown in Fig. 5e.

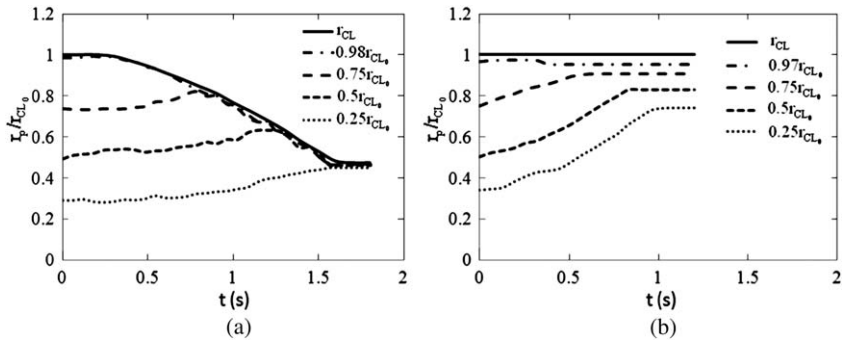

Fig. 4 Scaled radial position of microparticles *versus* time in an evaporating drop on substrates of different wettabilities. (a) $\theta_{RCA} = 55°$ and (b) $\theta_{RCA} = 10°$.

Eventually when enough rows of particles assemble near the CL, the friction force acting on the particles overcomes the surface tension force. Particles are then pinned near the CL to facilitate CL pinning, and hence the mixed mode of evaporation is reached. However, as most of the carrier liquid has already evaporated in the first two stages, the remaining liquid does not allow particles to separate according to their sizes. This mixed deposition of micro- and nanoparticles can be seen in the top-view image of the final deposit obtained by scanning electron microscopy (Fig. 6a) and the bottom-view image using fluorescence microscopy (Fig. 6b). As the constant contact angle mode dominates the entire evaporation process for the case of a large

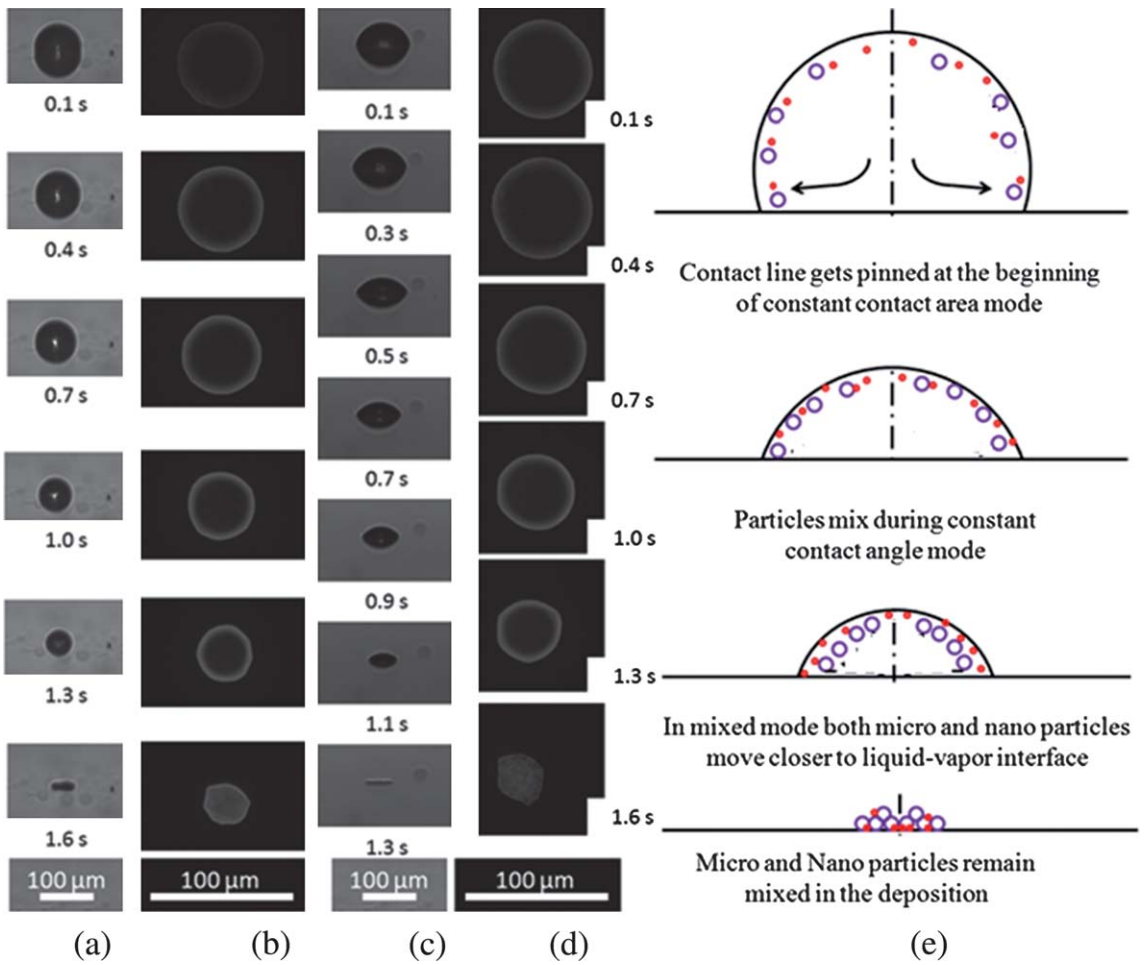

Fig. 5 Deposition dynamics of bi-dispersed particles from an evaporating colloidal drop on a glass substrate of $\theta_{RCA} > 45°$. (a) Snapshots from side view and (b) snapshots from bottom view on a glass substrate of $\theta_{RCA} = 80°$. (c) Snapshots from side view and (d) snapshots from bottom view on a glass substrate of $\theta_{RCA} = 55°$. (e) Schematic of the evaporation process. Colloidal suspension was formed from 0.1 and 1.1 µm polystyrene beads with a particle volume fraction of 0.5% each in water and the drop diameter before impact was 80 µm.

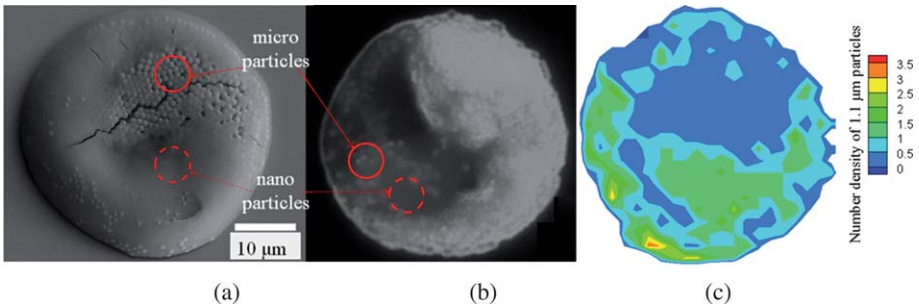

Fig. 6 Deposition morphology of bi-dispersed particles on a glass substrate of $\theta_{RCA} = 80°$. (a) SEM image (top view) and (b) fluorescence microscopy image (bottom view). Patches containing micro- and nanoparticles are indicated by solid and dashed circles respectively. (c) Average number density distribution of microparticles inside three deposited drops (based on top-view SEM images). Colloidal solution was formed from 0.1 and 1.1 μm polystyrene beads with a particle volume fraction of 0.5% each in water and the drop diameter before impact was 80 μm.

receding contact angle, the mixed mode of evaporation is very short as shown in Fig. 5a (side view) and b (bottom view) for $\theta_{RCA} = 80°$. As the wettability of the substrate increases to $\theta_{RCA} = 55°$ shown in Fig. 5c, a short film evaporation stage is observed after $t = 1.3$ s, where no observable changes are detected from the side-view images but the bottom-view images of drop evaporation reveal the assembly of particles until the water is completely dried. A contour map indicating the number density distribution of 1.1 μm particles is shown in Fig. 6c, obtained by averaging scanning electronic microscopy images of three bi-dispersed depositions on a glass substrate of $\theta_{RCA} = 80°$. As it can be observed from the figure, microparticles are distributed all across the deposited drop. Although the other part of the solid deposit is occupied by nanoparticles that are difficult to visualize individually, from the microparticle number density map, we conclude that the bi-dispersed particles are well mixed in the deposit.

B. $0° < \theta_{RCA} < 45°$ (partial separation)

For a substrate of $0° < \theta_{RCA} < 45°$, depending upon the interplay between the surface tension and friction forces acting on the particles, either all three stages or only the first stage of evaporation can be observed. In the case of $\theta_{RCA} = 30°$ as shown in Fig. 5a and b, where $F_s\cos\theta > fF_a$, all three stages of evaporation are observed. However, for $\theta_{RCA} = 10°$ shown in Fig. 5c and d, where $F_s\cos\theta < fF_a$, only the constant contact area mode can be

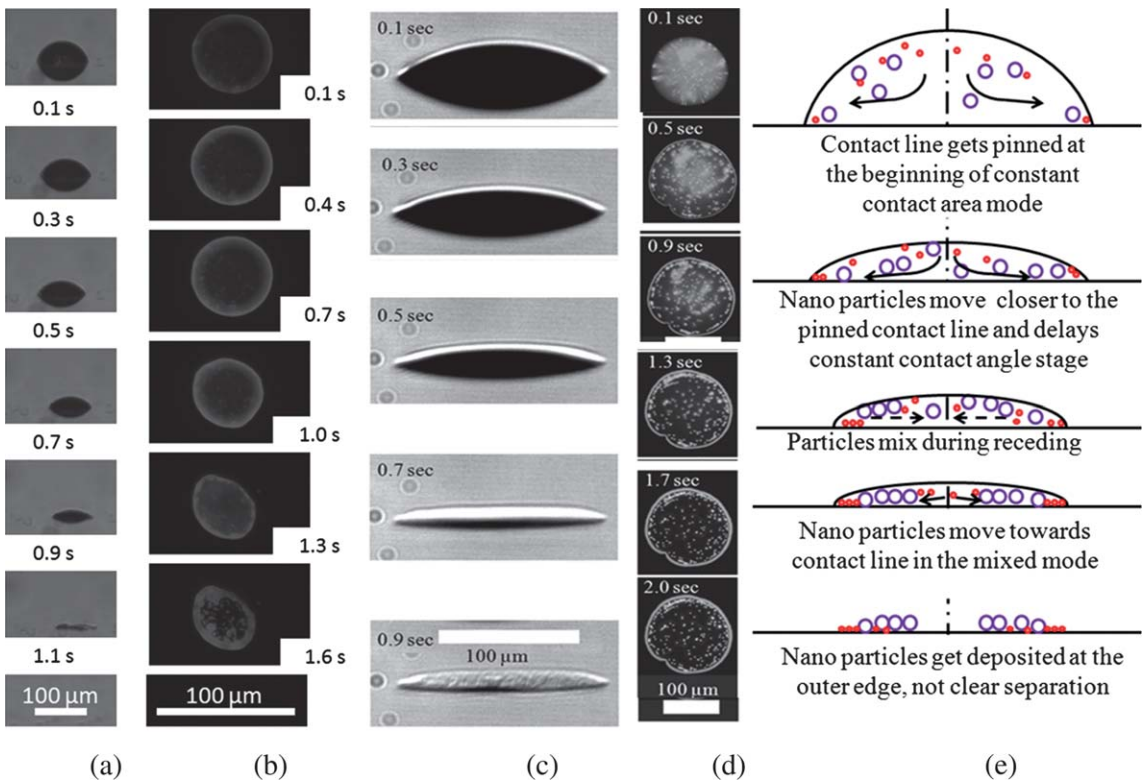

Fig. 7 Deposition dynamics of bi-dispersed particles on a glass substrate of $0 < \theta_{RCA} < 45°$. (a) Snapshots from side view and (b) snapshots from bottom view on a glass substrate of $\theta_{RCA} = 30°$. (c) Snapshots from side view and (d) snapshots from bottom view on a glass substrate of $\theta_{RCA} = 10°$. (e) Schematic of the evaporation process. Colloidal solution was formed from 0.1 and 1.1 μm polystyrene beads with a particle volume fraction of 0.5% each in water and the drop diameter before impact was 80 μm.

observed. After the drop reaches its maximum diameter (usually within 100 ms), the CL pins due to heterogeneities on the substrate. Due to a higher evaporation rate near the CL, particles are advected near the CL region and enhance CL pinning.[20-22] For a substrate of $0^\circ < \theta_{RCA} < 45^\circ$, depending upon the interplay between the surface tension and friction forces acting on the particles, either all three stages or only the first stage of evaporation can be observed. In the case of $\theta_{RCA} = 30^\circ$ as shown in Fig. 7a and b, where $F_s\cos\theta > fF_a$, all three stages of evaporation are observed. However, for $\theta_{RCA} = 10^\circ$ shown in Fig. 7c and d, where $F_s\cos\theta < fF_a$, only the constant contact area mode can be observed. After the drop reaches its maximum diameter (usually within 100 ms), the CL pins due to heterogeneities on the substrate. Due to a higher evaporation rate near the CL, particles are advected near the CL region and enhance CL pinning.[20-22] However, as shown in Fig. 1b, as the contact angle decreases during the constant contact area stage of evaporation, a higher number of particles (~100 rows) is required near the CL to maintain particle pinning. Two subsequent scenarios occur. If particles cannot form enough number of rows to pin, the CL begins to recede once the dynamic contact angle reaches θ_{RCA}. During the constant contact angle stage, the drop evaporates uniformly along the liquid–vapor interface and the surface tension force acting on the particles at the receding liquid–vapor interface pulls the particles along with it. The interplay of surface tension and friction forces depins particles near the CL. During the mixed mode of evaporation shown in Fig. 7a, as the contact angle decreases with time, more particles are required to overcome the surface tension force to maintain particle pinning. Particles keep moving inward until they accumulate to the minimum number required to pin at about 1.3 s as shown in Fig. 7b. However, if the number of particles in the CL region is larger than that is required for particle pinning to occur at all times, particles near the CL will remain pinned as shown in Fig. 7c and d. This further facilitates contact line pinning and for this scenario, the contact angle continuously decreases until it reaches 0°. In both scenarios (Fig. 7a and b *versus* Fig. 7c and d), no observable changes are detected from the side-view images after $\theta < 5^\circ$ (*i.e.*, after $t = 1.1$ s and $t = 0.9$ s in Fig. 7a and c, respectively) due to film evaporation at the very late stage,[15] where the bottom-view images of evaporation reveal assembly of particles until the water is completely dried.

As shown in Fig. 7c and d, when the CL is pinned, the CL wedge restricts the movement of microparticles closer to the edge of the drop compared to their nano-sized counterparts. As nanoparticles are 1000 times more in number compared to microparticles of the same volume fraction, more nanoparticles reach the CL region and enhance CL pinning. As the constant contact area mode is prolonged for this case, enough microparticles quickly assemble near the CL to pin themselves. However, for both cases of $\theta_{RCA} = 30^\circ$ and $\theta_{RCA} = 10^\circ$, particle separation near the CL is incomplete in the final deposition, where, from the outermost to the center of the drop is a region containing only nanoparticles, a region having overlap of micro- and nanoparticles, and an inner ring consisting of only microparticles. The interplay of surface tension and friction forces acting on particles determines the width of the middle region where micro- and nanoparticles overlap. Particle separation improves when the width of this mixed region decreases at a low θ_{RCA}, where the friction force overcomes the surface tension force.

C. $\theta_{RCA} = 0^\circ$ (complete separation)

For a hydrophilic substrate of $\theta_{RCA} = 0$, the drop CL remains pinned during the entire evaporation and only the drop contact angle decreases with time as shown in Fig. 8a. The liquid–vapor interface forms a wedge-like shape near the pinned CL and particles are advected towards the CL due to a higher evaporative flux there.[20–22] As the friction force increases due to continuous accumulation of nanoparticles near the CL, it overcomes the surface tension force acting on these particles resulting in pinning of nanoparticles along the CL. The bottom-view images in Fig. 8b show the assembly of nanoparticles in more than a hundred rows along the CL, preventing the drop from receding. A strong evaporative flow advects microparticles towards the pinned CL and due to the large momentum of these microparticles, some of them protrude through the liquid–vapor interface. This reduces the surface tension force acting on protruded microparticles compared with the value determined by eqn (9), such that the surface tension force cannot overcome the friction force to move the particles radially inward. After 0.5 s, no change can be observed from the drop side-view images in Fig. 8a, but

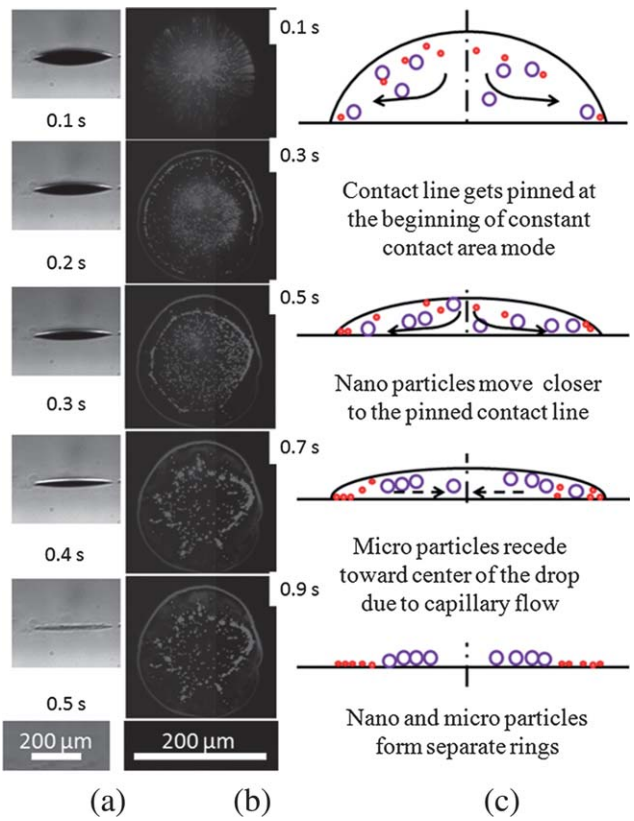

Fig. 8 Deposition dynamics of bi-dispersed particles on a glass substrates of $\theta_{RCA} = 0^\circ$. (a) Snapshots from side view and (b) snapshots from bottom view (particles marked by arrows do not recede inward after 0.5 s suggesting that they protrude through the liquid–vapor interface). (c) Schematic of the evaporation process. Colloidal solution was formed from 0.1 and 1.1 µm polystyrene beads with a particle volume fraction of 0.5% each in water and the drop diameter before impact was 80 µm.

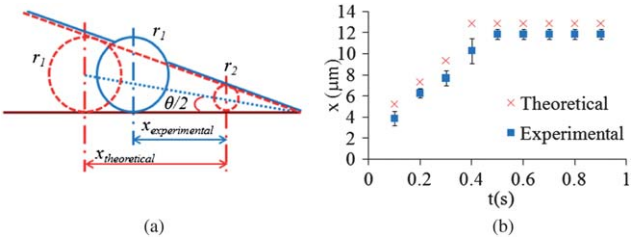

Fig. 9 Comparison of theoretically and experimentally determined particle separation distances of outermost micro- and nanoparticles on a substrate of $\theta_{RCA} = 0°$. (a) Schematic of the wedge assumption and micro-sized particle penetrating liquid–vapor interface and (b) theoretical and experimental particle separation distances as a function of time where the experimental separation distance is obtained based on three separate experiments and error bars denote the standard deviation.

the inward movement of microparticles can be seen in bottom-view images (Fig. 8b) until the drop is completely dried at 0.9 s. For a very hydrophilic substrate, microparticles cannot reach the minimum number of rows required to pin, and hence the surface tension acting on microparticles drives most of them moving radially inward to the center of the drop as shown in Fig. 8b. In the meantime, some microparticles do not move radially inward suggesting that they protrude through the liquid–vapor interface as indicated by arrows in Fig. 8b.

Similar to Perelaer *et al.*[4] and Biswas *et al.*[3] who used simple trigonometry based on the CL wedge assumption to estimate the distance of the outermost particles from the CL for an inkjet-printed mono-dispersed colloidal drop, the separation distance x of the outermost micro- and nanoparticles can be calculated by:

$$x_{\text{theoretical}} = \frac{(r_1 - r_2)}{\tan(\theta/2)} \quad (10)$$

where r_1 and r_2 are 550 and 50 nm respectively. Fig. 9 shows the theoretically estimated and experimentally measured separation distances as a function of time. As the drop spreads to a larger area on a hydrophilic substrate, surface irregularities reduce the drop circularity and lead to large experimental variations (~12%) in the final deposition morphology. However, it can be observed that, for the entire evaporation process, the measured separation distance is smaller than that suggested by the CL wedge assumption; this discrepancy indicates that some micro-sized particles protrude through the liquid–vapor interface due to the strong evaporatively driven flow inside the drop and shorten the particle separation distance.

5. Conclusions

In this paper, the deposition behavior of an inkjet-printed aqueous colloidal drop consisting of bi-dispersed micro- and nanoparticles has been investigated using fluorescence microscopy for glass substrates of varying wettabilities. The surface tension, electrostatic, drag, and van der Waals forces acting on particles near the CL have been estimated. With the change in substrate wettability θ_{RCA} from 85° to 0°, significant differences are observed in the duration of the three evaporation modes whose corresponding microflow patterns inside the drop result in different particle dynamics and deposition morphologies of bi-dispersed colloidal drops. For a hydrophobic substrate, the constant contact angle stage dominates the entire evaporation process, leaving very little carrier liquid left to rearrange particles according to their sizes at the mixed mode such that the micro- and nanoparticles mix well in the final deposition. For a hydrophilic substrate of $0° < \theta_{RCA} < 45°$, particle separation is incomplete in the final deposition. Three separate regions exist from the outermost to the center of the drop including a region with only nanoparticles, a mixture of micro- and nanoparticles, and an inner region with only microparticles. The width of the middle region where micro- and nanoparticles overlap depends upon the interplay of the surface tension and friction forces acting on the particles. For a hydrophilic substrate of $\theta_{RCA} = 0$, nanoparticles accumulate at the CL forming a large number of rows (>~100) that prevent CL from receding. This enhanced pinning by nanoparticles permits radially outward evaporative flow toward the pinned CL and pushes some of the microparticles to protrude through the liquid–vapor interface. Reduced surface tension acting on those protruded microparticles prevents them from moving inward, whereas most other microparticles move radially inward to the center of the drop at the late stage of evaporation when enough number of particles required to pin is reached. By modifying substrate wettability, the surface tension force acting on the particles is tuned. The control of particle separation according to their sizes can therefore be achieved.

We have also found that the increase in the size ratio of the bi-dispersed particles improves particle separation. As the number of particles affects CL pinning, the boundaries between mixed, partially separated, and completely separated regimes shift toward a higher θ_{RCA} value for a higher particle loading. The relative humidity of the environment also influences the separation distance of bi-dispersed particles. As reported in our earlier paper,[15] a lower relative humidity (higher evaporation rate) will result in a higher contact angle. This leads to poor particle separation as compared to drop evaporating in a high humidity environment. Hence, by controlling the substrate wettability, particle size ratio, particle loading, and relative humidity, the deposition morphology of bi-dispersed particles can be further controlled.

Acknowledgements

Support for this work was provided by the National Science Foundation (grant no. CAREER-0968927). We thank Dr Abhijit Joshi for fruitful discussions.

References

1 J. H. Kim, S. I. Ahn, J. H. Kim and W. C. Zin, *Langmuir*, 2007, **23**, 6163.
2 A. S. Sangani, C. Lu, K. Su and J. A. Schwarz, *Phys. Rev. E: Stat., Nonlinear, Soft Matter Phys.*, 2009, **80**, 011603.
3 S. Biswas, S. Gawande, V. Bromberg and Y. Sun, *J. Sol. Energy Eng.*, 2010, **132**, 021010.
4 J. Perelaer, P. J. Smith, C. E. Hendriks, A. M. J. van den Berg and U. S. Schubert, *Soft Matter*, 2008, **4**, 1072.
5 J. Y. Jung and H. Y. Kwak, *Anal. Chem.*, 2007, **79**, 5087.
6 J. Y. Jung, W. K. Young and Y. Y. Jung, *Anal. Chem.*, 2009, **81**, 8256.
7 J. Y. Jung, Y. W. Kim, J. Y. Yoo, J. Koo and Y. T. Kang, *Anal. Chem.*, 2010, **82**, 784.

8 C. S. Hodges, Y. Ding and S. Biggs, *J. Colloid Interface Sci.*, 2010, **352**, 99.
9 T. S. Wong, T. H. Chen, X. Shen and C. M. Ho, *Anal. Chem.*, 2011, **83**, 1871.
10 C. C. Monteux and F. O. Lequeux, *Langmuir*, 2011, **27**, 2917.
11 B. M. Weon and J. H. Je, *Phys. Rev. E: Stat., Nonlinear, Soft Matter Phys.*, 2010, **82**, 015305.
12 W. Han, M. Byun and Z. Lin, *J. Mater. Chem.*, 2011, DOI: 10.1039/c1jm11603g.
13 C. Poulard, O. Bénichou and A. M. Cazabat, *Langmuir*, 2003, **19**, 8828.
14 K. S. Birdi, D. T. Vu and A. Winter, *J. Phys. Chem.*, 1989, **93**, 3702.
15 V. H. Chhasatia, A. S. Joshi and Y. Sun, *Appl. Phys. Lett.*, 2010, **97**, 231909.
16 M. Elimelech, J. Gregory, X. Jia and R. A. Williams, *Particle Deposition & Aggregation*, Butterworth Heinemann publications, Woburn, MA, 1998.
17 R. Hogg, T. W. Healy and D. W. Fuerstenau, *Trans. Faraday Soc.*, 1966, **62**, 1638.
18 J. Visser, *Adv. Colloid Interface Sci.*, 1972, **3**, 331.
19 D. M. Kuncicky and O. D. Velev, *Langmuir*, 2008, **24**, 1371.
20 R. D. Deegan, O. Bakajin, T. F. Dupont, G. Huber, S. R. Nagel and T. A. Witten, *Nature*, 1997, **389**, 827.
21 J. Xu, J. Xia, S. Hong, Z. Lin, F. Qiu and Y. Yang, *Phys. Rev. Lett.*, 2006, **96**, 066104.
22 J. Xu, J. Xia and Z. Lin, *Angew. Chem., Int. Ed.*, 2007, **46**, 1860.